Surface & Coatings Technology 442 (2022) 128235

Contents lists available at ScienceDirect

Surface & Coatings Technology

journal homepage: www.elsevier.com/locate/surfcoat

Probing the onset of wurtzite phase formation in (V,Al)N thin films by transmission electron microscopy and atom probe tomography

Marcus Hans [a], Zsolt Czigány [b,*], Deborah Neuß [a], Janis A. Sälker [a], Holger Rueß [a], Janina Krause [a,1], Ganesh K. Nayak [c], David Holec [c], Jochen M. Schneider [a]

[a] Materials Chemistry, RWTH Aachen University, Kopernikusstr. 10, D-52074 Aachen, Germany
[b] Institute for Technical Physics and Materials Science, Centre for Energy Research, Konkoly-Thege Miklós út 29-33, H-1121 Budapest, Hungary
[c] Department of Materials Science, Montanuniversität Leoben, Franz-Josef-Str. 18, A-8700 Leoben, Austria

ARTICLE INFO

Keywords:
Transition metal aluminum nitrides
Thermal stability
Nucleation and growth
Density functional theory
Mechanical properties

ABSTRACT

Single-phase metastable cubic (V,Al)N thin films with columnar microstructure were grown by high power pulsed magnetron sputtering at 440 °C and the thermal decomposition mechanisms were systematically investigated by post-deposition vacuum annealing from 600 to 900 °C. The onset of spinodal decomposition into isostructural V- and Al-rich cubic nitride phases is demonstrated after cyclic vacuum annealing at 700 °C. Moreover, at this temperature, evidence for aluminum diffusion to grain boundaries and triple junctions is provided by correlation of transmission electron microscopy and atom probe tomography data. The formation of Al-rich regions can be understood by the more than 25% lower activation energy for bulk diffusion of aluminum compared to vanadium as obtained from ab initio calculations. It is reasonable to assume that these Al-rich regions are precursors for the formation of wurtzite AlN, which is unambiguously identified after annealing at 800 °C by microscopy and tomography. The significantly larger equilibrium volume of wurtzite AlN compared to the cubic phase explains its initial formation exclusively at triple junctions and grain boundaries. In contrast, twin boundaries are enriched in vanadium. Interestingly, the formation of the wurtzite phase at grain boundaries and triple junctions can be tracked by resistivity measurements, while X-ray diffraction and nanoindentation data do not support an unambiguous wurtzite phase formation claim for annealing temperatures <900 °C. Hence, it is evident that previously reported formation temperatures of wurtzite AlN in transition metal aluminum nitrides, determined by other characterization techniques than chemical and structural characterization at the nanometer scale and/or resistivity measurements, are overestimated.

1. Introduction

The incorporation of aluminum in titanium nitride in 1986 [1] paved the way for the application of wear-resistant thin films on tools and components [2]. Metastable transition metal aluminum nitrides with cubic crystal structure (space group $Fm\bar{3}m$, NaCl prototype) exhibit excellent mechanical properties, induced by the mixture of covalent, ionic and metallic bonds [3]. The bond strength is significantly affected by the transition metal: bulk modulus values of approximately 261, 280 and 234 GPa were predicted for $Ti_{0.5}Al_{0.5}N$, $V_{0.5}Al_{0.5}N$ and $Cr_{0.5}Al_{0.5}N$, respectively [4]. Enhancement of elastic properties from $Ti_{0.5}Al_{0.5}N$ to $V_{0.5}Al_{0.5}N$ can be understood based on the electronic structure as the length of transition metal-nitrogen bonds is reduced from 2.13 Å (Ti-N) to 2.06 Å (V-N) [5].

Recently, systematic variations of the aluminum content in $V_{1-x}Al_xN$ were studied by density functional theory: incorporation of $x = 0$ to 0.75 caused 26% enhancement of the elastic modulus from 388 to 488 GPa and was explained by strong sp^3d^2 hybridization between aluminum and nitrogen, inducing the formation of covalent bonds [6]. Experimentally, a large range of elastic modulus values has been reported between 254 GPa ($x = 0$) [7] and 599 GPa ($x = 0.52$) [8]. Hence, it is evident that besides the aluminum content, also the residual stress state, nitrogen

* Corresponding author.
E-mail addresses: hans@mch.rwth-aachen.de (M. Hans), czigany.zsolt@ek-cer.hu (Z. Czigány), neuss@mch.rwth-aachen.de (D. Neuß), saelker@mch.rwth-aachen.de (J.A. Sälker), janina.krause@speira.com (J. Krause), ganesh.nayak@unileoben.ac.at (G.K. Nayak), david.holec@unileoben.ac.at (D. Holec), schneider@mch.rwth-aachen.de (J.M. Schneider).
[1] Present address: Speira GmbH, Aluminiumstr. 1, D-41515 Grevenbroich, Germany.

https://doi.org/10.1016/j.surfcoat.2022.128235

Available online 10 February 2022

concentration as well as impurities strongly affect experimentally measured elastic modulus values of $V_{1-x}Al_xN$ [6].

While the above discussed experimental elastic properties were determined at room temperature, wear-resistant thin films are exposed to high temperatures and compressive stresses of up to 900 °C and 2 GPa, respectively [9]. Thus, the metastable solid solution phase must be preserved at elevated temperatures. Thermal decomposition can occur by spinodal decomposition [10,11] or nucleation and growth of wurtzite AlN (space group $P6_3mc$). In case of (Ti,Al)N the formation of wurtzite AlN results in degradation of mechanical properties [12], while spinodal decomposition does not reduce the mechanical properties [13]. The presence of wurtzite AlN in metastable cubic solid solutions is commonly identified by structural characterization [14].

We have recently demonstrated the concurrent spinodal decomposition as well as nucleation and growth of wurtzite AlN in single-phase metastable cubic $(V_{0.64}Al_{0.36})_{0.49}N_{0.51}$ thin film flakes after vacuum annealing at 900 °C [15]. However, lower annealing temperatures have not been investigated. Based on our recent findings [15] the onset temperature of thermal decomposition is ≤900 °C. Moreover thin film flakes, obtained by deposition on NaCl substrates and dissolving the substrate in water [15], did not allow for characterization of the mechanical properties.

In the present work, the thermal stability of $(V_{0.64}Al_{0.36})_{0.49}N_{0.51}$ thin films with columnar microstructure is systematically investigated by vacuum annealing from 600 to 900 °C. Thermal decomposition is assessed by X-ray diffraction, transmission electron microscopy techniques, atom probe tomography as well as nanoindentation and resistivity measurements. Based on diffraction and nanoindentation data, the onset of wurtzite AlN phase formation is found after annealing at 900 °C. However, correlation of transmission electron microscopy and atom probe tomography data provides evidence for aluminum diffusion to grain boundaries and triple junctions already after annealing at 700 °C. The formation of Al-rich regions can be understood by the more than 25% lower activation energy for bulk diffusion of aluminum compared to vanadium as obtained from ab initio calculations. It is reasonable to assume that these segregations are precursors for wurtzite phase formation after annealing at 800 °C.

2. Experimental details

Prior to thin film growth, 10 × 10 mm sapphire (0001) substrates were annealed at 1100 °C in ambient atmosphere in order to remove residuals from the polished surface. These substrates were positioned at a distance of 4.5 cm from a $V_{0.6}Al_{0.4}$ target (>99.7% purity) which was produced by Plansee Composite Materials GmbH. The CemeCon CC800/9 deposition system was evacuated to a base pressure $< 5 \times 10^{-4}$ Pa and the substrates were heated to 440 °C as measured by a thermocouple (NiCr-Ni, K type) clamped to the substrate holder. High power pulsed magnetron sputtering was carried out with a Melec SIPP2000USB-10-500-S power supply, employing pulse on- and off-time of 50 and 1950 μs, respectively, at time-average power of 2 kW and peak power density of 0.5 kW cm^{-2}. A 50 nm adhesion layer was formed with 160 sccm Ar for the first 30 s of film growth to enhance adhesion and subsequently 55 sccm of N_2 was introduced. The deposition pressure was 0.4 Pa with 0.1 Pa partial pressure of N_2. The total deposition time was 60 min, resulting in a film thickness of 2.6 μm. Venting of the deposition system was done at temperatures <100 °C in order to reduce surface oxidation [16]. The chemical composition of $(V_{0.64}Al_{0.36})_{0.49}N_{0.51}$ (impurities of 0.5 at.% O and 0.4 at.% C), with a measurement uncertainty of ~2.5 at.% for nitrogen and aliquot fractions for vanadium and aluminum, was obtained by combination of time-of-flight elastic recoil detection analysis and Rutherford backscattering spectrometry [15]. The growth conditions were identical to the synthesis of thin film flakes reported in [15].

Vacuum annealing was carried out in a high vacuum furnace with base pressure of $< 3 \times 10^{-4}$ Pa. Since for each heat treatment the identical thin film was used, it is referred to as cyclic annealing in the following. The temperature was varied systematically from 600 to 700, 800 and 900 °C and the heating rate as well as the dwell time were always 10 °C min^{-1} and 30 min, respectively. At 900 °C, the base pressure increased up to 9×10^{-3} Pa. The temperature was measured with a thermocouple (PtRh-Pt, S type) positioned in the hot zone of the furnace and the venting temperature was <50 °C to avoid additional surface oxidation [16].

Structural analysis of as deposited and annealed thin films was carried out by X-ray diffraction. Phase formation was investigated by θ-2θ scans in Bragg-Brentano geometry (Siemens D5000 system) with 1° offset to avoid signal from the single crystal (0001) substrate as well as in fixed incidence angle ($\omega = 15°$) geometry (Bruker AXS D8 Discover General Area Diffraction Detection System). The 2θ range from 20 to 80° was scanned at a step size of 0.05° for both setups. Stress-free lattice parameters as well as residual stresses were measured by the $\sin^2(\Psi)$ method [17]. The d spacing of the (111) lattice plane was studied in Bragg-Brentano geometry. Assuming a biaxial stress state, the strain-free tilt angle of 35.26° was obtained based on the Poisson's ratio [18] and used for evaluation of stress-free lattice parameters. The residual stress state was quantified with elastic modulus values from nanoindentation. A Poisson's ratio ν of 0.23 was obtained by linear interpolation of data published in [6,19]. The Cu X-ray sources of both systems were operated at voltage and current of 40 kV and 40 mA, respectively.

Elastic modulus and hardness were determined by quasistatic nanoindentation in a Hysitron TI-900 TriboIndenter using the method from Oliver and Pharr [20]. 10 mN were applied in load-controlled measurement mode to a diamond tip ($\nu = 0.07$, $E = 1140$ GPa) with Berkovich geometry and the maximum contact depth was 120 nm. 25 indents were performed for each cyclic annealing condition. The tip area function was derived from measurements on fused silica and as deposited $(V_{0.64}Al_{0.36})_{0.49}N_{0.51}$ was used as reference for each nanoindentation measurement series in order to ensure comparability of testing conditions since blunting of the triangular tip may result in up to 3.4% uncertainty of elastic modulus [21]. Measured indentation modulus values were converted to the elastic modulus with a Poisson's ratio ν of 0.23 as mentioned above.

Resistivity measurements were carried out by a Van der Pauw setup [22] using a Keithley 2611B System SourceMeter with a current of 5 mA. Three sets of measurements were done at room temperature and ambient atmosphere for each cyclic annealing condition.

Thin lamellae for transmission electron microscopy as well as atom probe specimens were prepared by focused ion beam techniques using a FEI Helios Nanolab 660 dual-beam microscope at 30 kV voltage. Final thinning of the lamellae was carried out with a Thermo Scientific Scios 2 dual-beam at 2 kV. For the atom probe specimens a standard protocol was employed and final annular milling of the needle-shaped specimens was done at 5 kV [23]. Lift-outs were done from the thin film surfaces (referred to as cross-section in the following) as well as from fracture cross-sections with <500 nm distance from the thin film surface (referred to as plan-view in the following). Both lift-out geometries are schematically shown in Fig. S1 in the Supplementary material.

Transmission electron microscopy was performed in a C_s-corrected 200 kV Thermo Fisher Themis microscope with 0.8 Å resolution. Bright field (BF) and dark field (DF) images were acquired and selected area electron diffraction (SAED) was done. Moreover, high angle annular dark field (HAADF) images were acquired in scanning transmission electron microscopy (STEM) mode and elemental maps were obtained from energy dispersive X-ray spectroscopy (EDX) spectrum images.

Local chemical composition measurements at the nanometer scale were done by laser-assisted atom probe tomography using a CAMECA LEAP 4000X HR with an ultraviolet laser (pulse width of 10 ps). The laser pulse frequency, base temperature and detection rate were set at 200 kHz, 60 K and 0.5%. The laser pulse energy of 10 pJ was used in order to increase the electric field strength during evaporation and consequently the accuracy of absolute chemical compositions [24,25].

3. Computational details

Density functional theory, implemented in the Vienna Ab Initio Simulation Package (VASP) [26,27], was used to estimate the barriers for diffusion during decomposition. The generalized gradient approximation as implemented by Perdew-Burke-Ernzerhof [28] was employed for the electron-electron exchange and correlation potential. The pseudopotentials used for the elements treat semi-core states of V ([Ne] $3s^2 3p^6 4s^1 3d^4$), Al([Ne]$3s^2 3p^1$) and N($1s^2 2s^2 2p^3$) as valence states. Ion-electron interactions were described using the projector augmented wave method [29] with a plane-wave energy cutoff of 500 eV. A $2 \times 2 \times 2$ supercell (space group $Fm\bar{3}m$, NaCl prototype) with 64 atoms was used as a base model for defect-free $V_{1-x}Al_xN$, $x = 0.0$, 0.25, 0.5 and 1.0. Hence, the simulation box had a length below ~0.9 nm. Test calculations on the established TiN system were done and it was found that larger simulation boxes ($4 \times 4 \times 4$ supercell) do not significantly affect the results. The $x = 0.25$ and 0.5 compositions were modeled with the special quasi-random structures [30]. For these cubic supercells, a Monkhorst-Pack mesh [31] of $3 \times 3 \times 3$ k-points was used for the Brillouin zone sampling with a Methfessel-Paxton [32] smearing of 0.2 eV.

In order to quantify the compositional effect on the activation energy for bulk diffusion, we calculated energy barriers for jumps between stable and transition states for all species. All the considered barriers for the jumps were between first nearest neighbors on the respective sublattice (32 metal and 32 nitrogen atoms), i.e. their separation was $a/2\langle 110 \rangle$ with a being the conventional cubic lattice parameter. The procedure started by removing atoms one at a time, hence creating a set of 64 supercells each containing one vacancy. Each such state was completely relaxed with respect to internal degrees of freedom (ionic coordinates). The volume and shape for each defected state were kept unchanged and fixed to the values corresponding to a fully relaxed defect-free parent supercell without any vacancy. Afterwards, all possible pairs of initial and final jump states were identified. The energy of the transition state (saddle point) along the minimum energy diffusion path, connecting the initial and final states, was determined by a nudged elastic band [33] method, as implemented in VASP, with single image calculations.

4. Results and discussion

4.1. Phase formation

The evolution of phase formation as a function of cyclic annealing temperature is presented in Fig. 1a and b. In the as deposited state, the formation of a single-phase metastable cubic solid solution with a preferred (111) orientation is evident. While the first annealing cycle at 600 °C caused only a slight shift of the (111) lattice plane peak position from 37.10 to 37.15°, the second annealing cycle at 700 °C resulted in a pronounced shift to 37.52°. The stress-free lattice parameter (Fig. 1c) decreases from 4.178 Å in the as deposited state to 4.116 Å after cyclic annealing at 900 °C. While the experimental lattice parameter in the as deposited state is 1.7% larger than the predicted value of 4.108 Å from density functional theory calculations at 0 K temperature [15], the

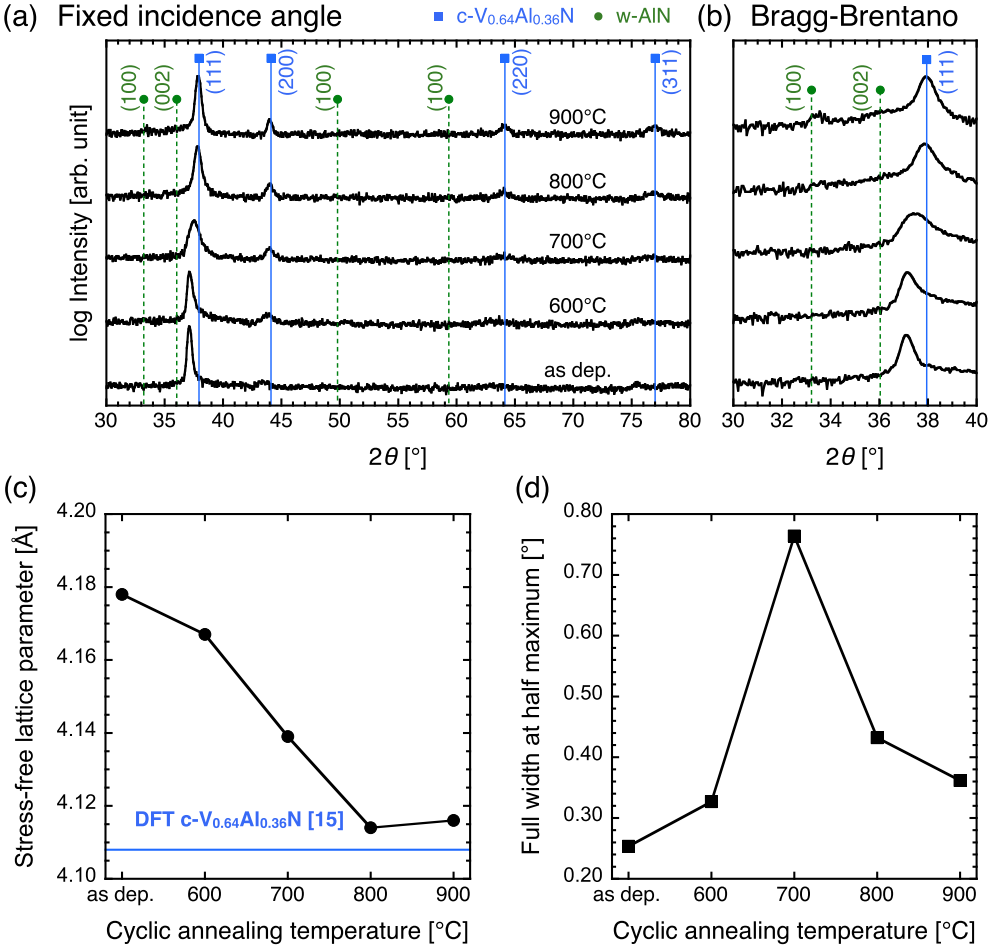

Fig. 1. Phase formation for different cyclic annealing temperatures. Diffractograms are shown from measurements (a) at fixed incidence angle and (b) in Bragg-Brentano geometry. (c) Stress-free lattice parameter and (d) full width at half maximum of the (111) lattice plane peak. The reference lines of cubic (c-) $V_{0.64}Al_{0.36}N$ (squares) and wurtzite (w-)AlN (circles) are taken from [15] and a card (00-025-1133) of the International Centre for Diffraction Data.

deviation is only 0.2% after annealing at 900 °C. XRD measurements were done at room temperature after annealing and the temperature difference of ~300 K between experimental and theoretical data causes an expansion of the lattice by 0.005 Å, based on extrapolation from the related material systems Ti-Al-N and Cr-Al-N [34]. Hence, it is reasonable to expect a temperature-induced uncertainty of 0.1% for the here employed V-Al-N lattice parameter predictions. It has been reported that the interstitial incorporation of one nitrogen atom in $Ti_{0.5}Al_{0.5}N$

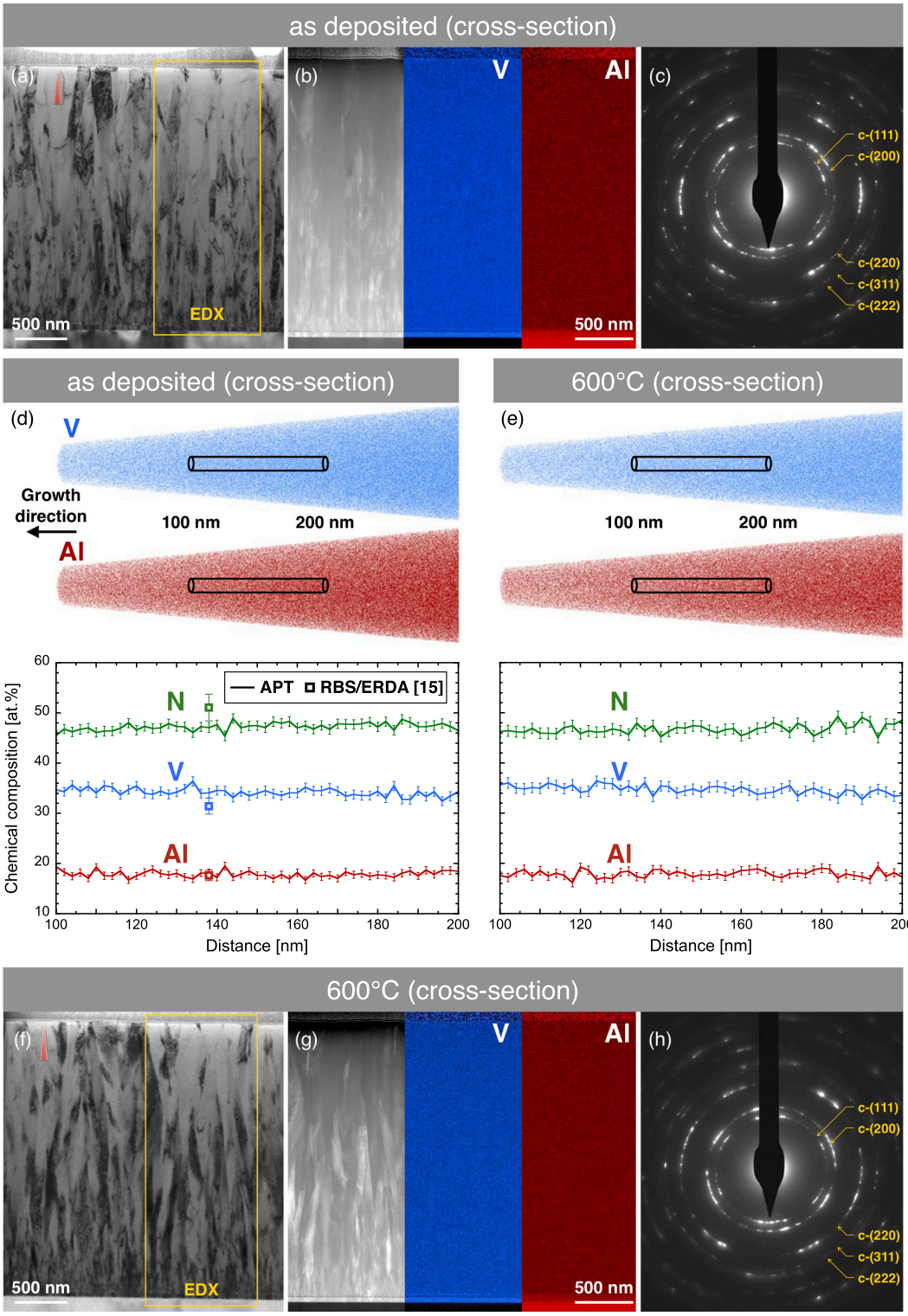

Fig. 2. Cross-section microstructure and local chemical composition in the as deposited state as well as after cyclic annealing at 600 °C. (a) BF image (as deposited). (b) HAADF and STEM-EDX elemental maps of V and Al (as deposited). The region of interest is indicated in (a). (c) SAED pattern (as deposited). APT reconstructions of V and Al atomic positions as well as chemical composition profiles from the cylinders with dimensions of 10 × 10 × 100 nm are shown for (d) the as deposited state as well as (e) after cyclic annealing at 600 °C. The data points in (d) correspond to ion beam analysis data from [15]. (f) BF image (600 °C). (g) HAADF and STEM-EDX elemental maps of V and Al (600 °C). The region of interest is indicated in (f). (h) SAED pattern (600 °C).

(supercell containing 32 metal and 32 nitrogen atoms) increases the lattice parameter by 0.9% [35]. In addition, the presence of 0.2% of aluminum Frenkel pairs was recently shown to increase the lattice parameter by 0.2% [36]. Hence, it is reasonable to assume that the deviation between the experimentally obtained lattice parameter and the ab initio prediction of a defect-free configuration is caused by the formation of defects: Firstly, as the here investigated films are slightly overstoichiometric, based on ion beam analysis data which provide an average chemical composition of $(V_{0.64}Al_{0.36})_{0.49}N_{0.51}$ [15], the formation of nitrogen interstitials during growth is likely to appear. Secondly, ion bombardment-induced formation of Frenkel pairs was reported to take place at ion energies ≥24 eV [36] and is thus relevant for the here employed growth conditions.

The evaluation of the full width at half maximum (Fig. 1d) emphasizes that the (111) peak width increases from 0.36° at 600 °C to 0.76° at 700 °C. An increase of the peak width has been observed upon spinodal decomposition of overstoichiometric (Ti,Al)N, while the formation of wurtzite AlN was accompanied by a decreasing full width at half maximum [37]. Hence, the peak broadening data indicate spinodal decomposition already after annealing at 700 °C, while wurtzite AlN phase formation is indicated after cyclic annealing at 900 °C from the small peak at approximately 33.5° (Fig. 1a and b).

4.2. Microstructure, chemical modulation and grain boundary composition

As deposited thin films exhibit a dense microstructure with columnar grain boundaries (Fig. 2a). The formation of elongated grains is caused by coalescence of islands and adatom surface diffusion which results in local epitaxial growth, shaping and extending the individual columns [38]. HAADF images and elemental maps from an area of 1 μm × 2.6 μm reveal the homogeneous composition distribution across the entire (V, Al)N thin film (Fig. 2b). Higher signals of vanadium and aluminum are obtained within the 50 nm metallic interlayer (between nitride film and sapphire substrate) which was applied to enhance adhesion. Electron diffraction data confirms the formation of a single-phase metastable cubic solid solution (Fig. 2c). Local chemical composition analysis provides evidence for the homogeneous distribution of vanadium as well as aluminum atoms at the nanometer scale in the as deposited state (Fig. 2d) as well as after cyclic annealing at 600 °C (Fig. 2e) and the respective compositional variations are within the count rate statistics. Moreover, the absolute chemical composition quantified by laser-assisted atom probe tomography is compared with ion beam analysis data [15]. In case of (Ti,Al)N the absolute nitrogen concentration from atom probe tomography data was underestimated by at least 5.5 at.% [25]. Similarly, the here observed underestimation of nitrogen by up to 4 at.% can be understood by the formation of non-detectable neutral fragments upon dissociation of molecular nitrogen-carrying ions during their flight towards the detector [39]. The microstructure after cyclic annealing at 600 °C does not show significant changes compared to the as deposited state (Fig. 2f–h). The fast Fourier transformation of a high resolution plan-view image (Fig. S2a–b in the Supplementary material) reveals only cubic reflections in agreement with electron diffraction data (Fig. 2c).

The microstructural characterization of a thin film cross-section, cyclically annealed at 700 °C (Fig. 3a–c), does not provide additional insights in comparison to the as deposited state as well as after annealing at 600 °C. However, the formation of Al-rich regions (≥30 at.%) is identified by chemical composition analysis at the nanometer scale from atom probe tomography data and highlighted by isoconcentration surfaces (Fig. 3d). The chemical composition profile from the metastable solid solution reveals anti-correlated variations of vanadium as well as aluminum between 28 and 34 as well as 18 and 26 at.%, respectively (Fig. 3e). These compositional variations are significantly larger than the count rate statistics and can be interpreted as the onset of spinodal decomposition in agreement with the significant peak broadening identified by X-ray diffraction (see Fig. 1d). Composition differences between a homogeneous matrix and chemically enriched regions can be evaluated by proximity histograms. In Fig. 3 (f) the evolution of the aluminum composition from the solid solution (distances <0 nm) to Al-rich regions (distances >0 nm) is presented for an aluminum threshold of 30 at.% (0 nm distance). The proximity histogram shows that aluminum is increased locally from approximately 20 at.% in the metastable solid solution up to 49 at.%, while vanadium is reduced from 33 to 12 at.%. The apparent reduction of the nitrogen content in the Al-rich region is most likely a measurement artefact. As the required evaporation field is lower in the Al-rich region (compared to the solid solution), the electric field strength and, consequently, the ionization probability of neutral nitrogen species is reduced in the Al-rich region [24]. Plan-view microstructural characterization (lamella extracted at <500 nm from the film surface) provides evidence for the diffusion of aluminum to the triple junctions via grain boundaries (Fig. 3g–h). Therefore, the linear feature of Al-rich regions in the cross-section atom probe reconstruction (compare Fig. 3d) relates most likely to a triple junction of the columnar grain boundaries. Moreover, V-rich (≥39 at.%) and Al-rich regions (≥27 at.%) are identified at the grain boundaries from the reconstruction of a plan-view atom probe specimen (Fig. 3i). The proximity histograms provide evidence that vanadium and aluminum are locally enriched at the grain boundaries and triple junctions up to 46 and 52 at.%, respectively (Fig. 3j and k).

A high resolution image of a grain boundary triple junction (Fig. S2c–d in the Supplementary material) was analyzed by fast Fourier transformation and besides cubic reflections, an additional spot with a lattice spacing of 1.32 Å was obtained which can be attributed to the wurtzite (112) reflection (see Table S1 in the Supplementary material). Consequently, the AlN-rich segregations at the triple junctions may have at least in part transformed from cubic to wurtzite structure, strengthening the notion that these regions act as precursors for wurtzite phase formation. This mechanism is consistent with the reported formation of nanocrystalline wurtzite AlN at grain boundary junctions of AlN/CrN superlattice thin films annealed in Ar at 900 °C [40].

After cyclic annealing at 800 °C, weak intensity (100) reflections of the wurtzite AlN phase are visible by electron diffraction (Fig. 4a). The HAADF image emphasizes contrast differences at the grain boundaries, especially close to the thin film surface (Fig. 4b). These dark regions correspond to aluminum enrichment as well as vanadium depletion (Fig. 4c). The fast Fourier transformation of a high resolution image (Fig. S2e–f in the Supplementary material) provides evidence for the wurtzite phase formation at the grain boundaries and triple junctions.

Atom probe specimens were prepared perpendicular to the film growth direction (plan-view) in order to increase the probability to capture a grain boundary (see indicated atom probe specimen volume in Fig. 4b). The reconstruction is presented with Al-rich (≥40 at.%) and V-rich (≥45 at.%) isoconcentration surfaces (Fig. 4d–e). These regions indicate the presence of a grain boundary in the atom probe dataset from a distance of 130 to 150 nm in the cylinder. Thus, an increase in the annealing temperature from 700 to 800 °C causes segregation of aluminum at the grain boundaries, while vanadium exhibits local agglomerations of up to 50 at.% in the grain boundary region. Since the nitrogen signal was homogeneous for the whole lamella, it can be inferred that the formation of VN-rich regions occurs subsequent to wurtzite AlN formation and is induced by aluminum diffusion. The incorporation of up to 8 at.% oxygen in the AlN-rich grain boundary (Fig. 4e) can be understood based on the formation of an Al_2O_3 phase which is energetically preferred over the formation of a metastable cubic oxynitride [41]. The fast Fourier transformation of a high resolution image (Fig. S2f in the Supplementary material) provides evidence for the local formation of thermodynamically stable α-Al_2O_3. Recently, it has been demonstrated that the presence of oxygen in (Ti,Al)(O,N) inhibits the formation of wurtzite AlN and is caused by the larger energy requirement to enable mobility on the oxynitride non-metal sublattice compared to the nitride [42]. Apart from the grain boundary, the

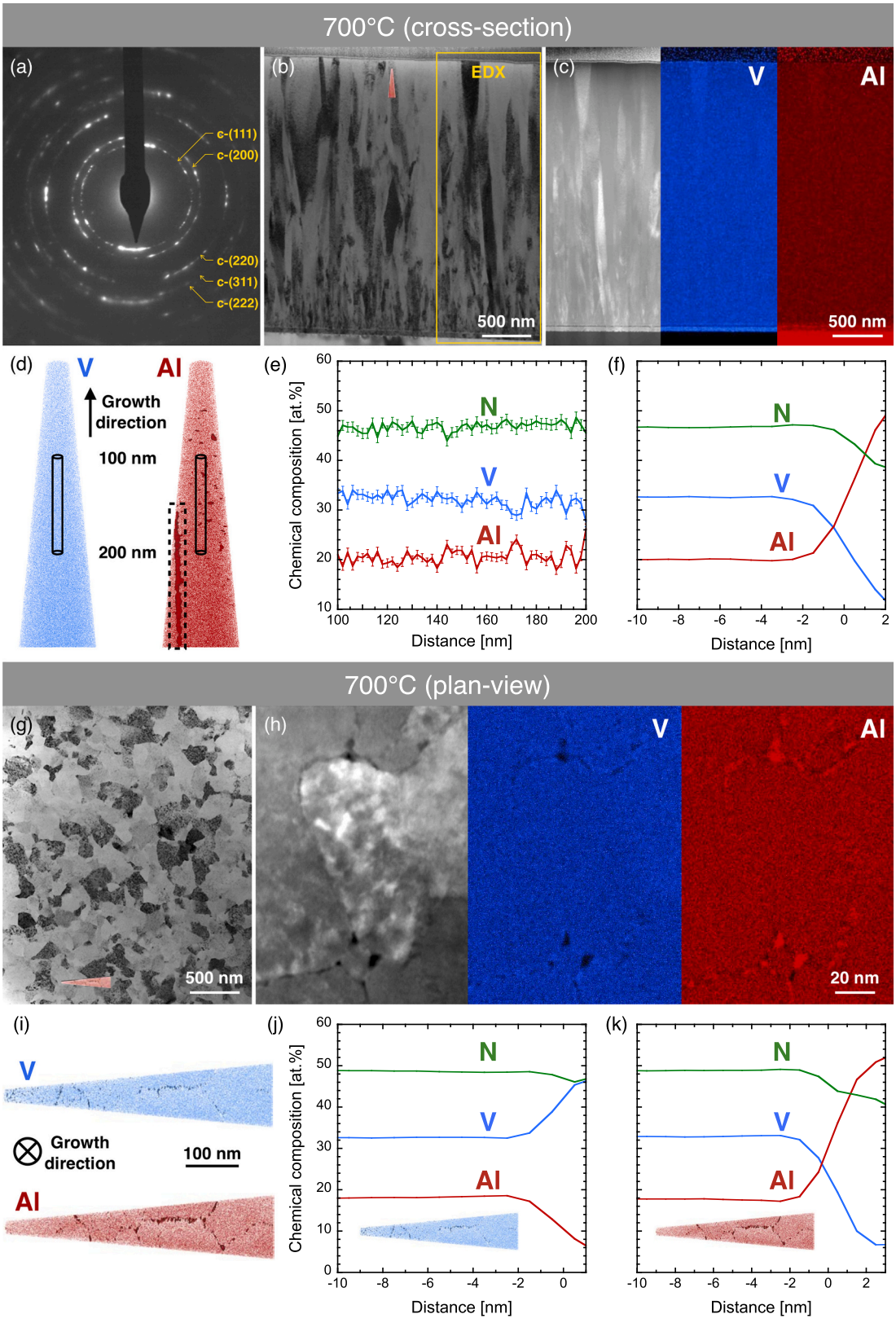

Fig. 3. Microstructure and local chemical composition after cyclic annealing at 700 °C. (a) SAED pattern (cross-section). (b) BF image (cross-section). (c) HAADF and STEM-EDX elemental maps of V and Al (cross-section). The region of interest is indicated in (b). (d) APT reconstruction of V and Al atomic positions (cross-section). Al-rich regions with ≥30 at.% are highlighted by isoconcentration surfaces. (e) Chemical composition profile from the cylinder with dimensions of 10 × 10 × 100 nm indicated in (d). (f) Proximity histogram of the Al-rich regions (≥30 at.%) highlighted with a dashed rectangle in (d). (g) BF image (plan-view). (h) HAADF and STEM-EDX elemental maps of V and Al (plan-view). (i) APT reconstruction of V and Al atomic positions (plan-view). V-rich regions with ≥39 at.% and Al-rich regions with ≥27 at.% are highlighted by isoconcentration surfaces. (j) Proximity histogram of the V-rich regions (≥39 at.%). (k) Proximity histogram of the Al-rich regions (≥27 at.%).

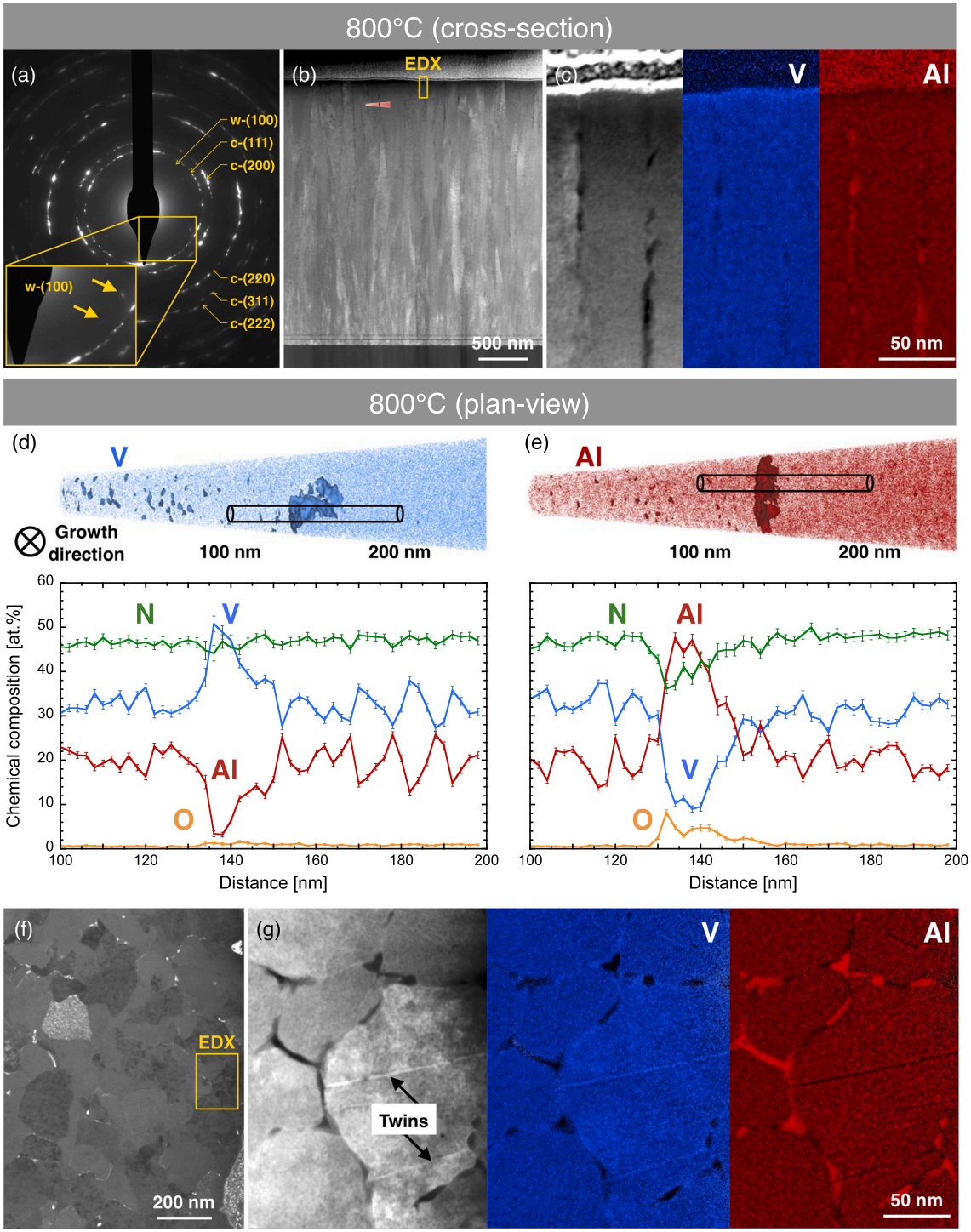

Fig. 4. Microstructure and local chemical composition after cyclic annealing at 800 °C. (a) SAED pattern (cross-section). The inset in (a) shows a magnified region to make the wurtzite (100) reflections visible. (b) HAADF image (cross-section). (c) HAADF and STEM-EDX elemental maps of V and Al (cross-section). The region of interest is indicated in (b). (d) APT reconstruction of V atomic positions (plan-view) and chemical composition profile from the cylinder with dimensions of 10 × 10 × 100 nm. V-rich regions with ≥45 at.% are highlighted by isoconcentration surfaces. (e) APT reconstruction of Al atomic positions (plan-view) and chemical composition profile from the cylinder with dimensions of 10 × 10 × 100 nm. Al-rich regions with ≥40 at.% are highlighted by isoconcentration surfaces. (f) DF image (plan-view) taken with the wurtzite (100) reflections. (g) HAADF and STEM-EDX elemental maps of V and Al (plan-view). The region of interest is indicated in (f).

chemical composition profiles demonstrate strong chemical composition modulations (distances of approximately 100 to 130 and 150 to 200 nm in the cylinders) of vanadium and aluminum in the range from 27 to 38 at.% and 13 to 26 at.%, respectively. The modulation wavelength is on the order of 6 to 10 nm and consistent with spinodal decomposition of the metastable solid solution into V- and Al-rich cubic nitride phases [15].

The plan-view dark field image taken with wurtzite (100) reflections (Fig. 4f) as well as elemental maps (Fig. 4g) emphasize the gradual formation of wurtzite AlN at the grain boundaries and triple junctions. Hence, these data are consistent with the aluminum enrichment observed by atom probe tomography and proof the subsequent wurtzite

AlN formation at the grain boundaries and triple junctions. In addition the presence of V-rich twin boundaries are observed by combination of HAADF images and elemental maps (Fig. 4g) as well as high-resolution images (Fig. S3 in the Supplementary material). Twin boundaries have been identified in magnetron-sputtered TiN at a substrate bias potential of −40 V and attributed to a reduction in stacking fault energy caused by the presence of nitrogen vacancies [43]. Density functional theory calculations were used for the prediction of stacking fault energies at 0 K and energies of cubic VN as well as TiN were at least a factor of four smaller than of cubic AlN [44]. Based on these stacking fault energy predictions, it can be understood that the twin boundaries are aluminum-depleted.

After cyclic annealing at 900 °C the intensity of the wurtzite phase (100) signal has increased (Fig. 5a). Dark field images were acquired with cubic (111) and (200) (Fig. 5b) as well as wurtzite (100) reflections (Fig. 5c). While the cubic phase can be observed within the grains, the entire thin film is decorated with wurtzite crystallites along the grain boundaries (Fig. 5c–d). Local chemical composition analysis emphasizes the massive formation of Al-rich regions (Fig. 5e–f) and spinodal decomposition causes chemical composition modulations of vanadium as well as aluminum in the range from 16 to 33 at.% as well as 17 to 39 at.%, respectively (Fig. 5g). The cyclic annealing of (V,Al)N thin films up to 900 °C induced similar compositional modulations as in thin film flakes after annealing at 1100 °C [15]. The here obtained strong decomposition at 200 °C lower temperature can be explained by the thermal history of cyclically annealed thin films (e.g. the thin film annealed at 900 °C had already experienced heat treatments at 600, 700 and 800 °C), while the thin film flakes were only subject to single heat treatments.

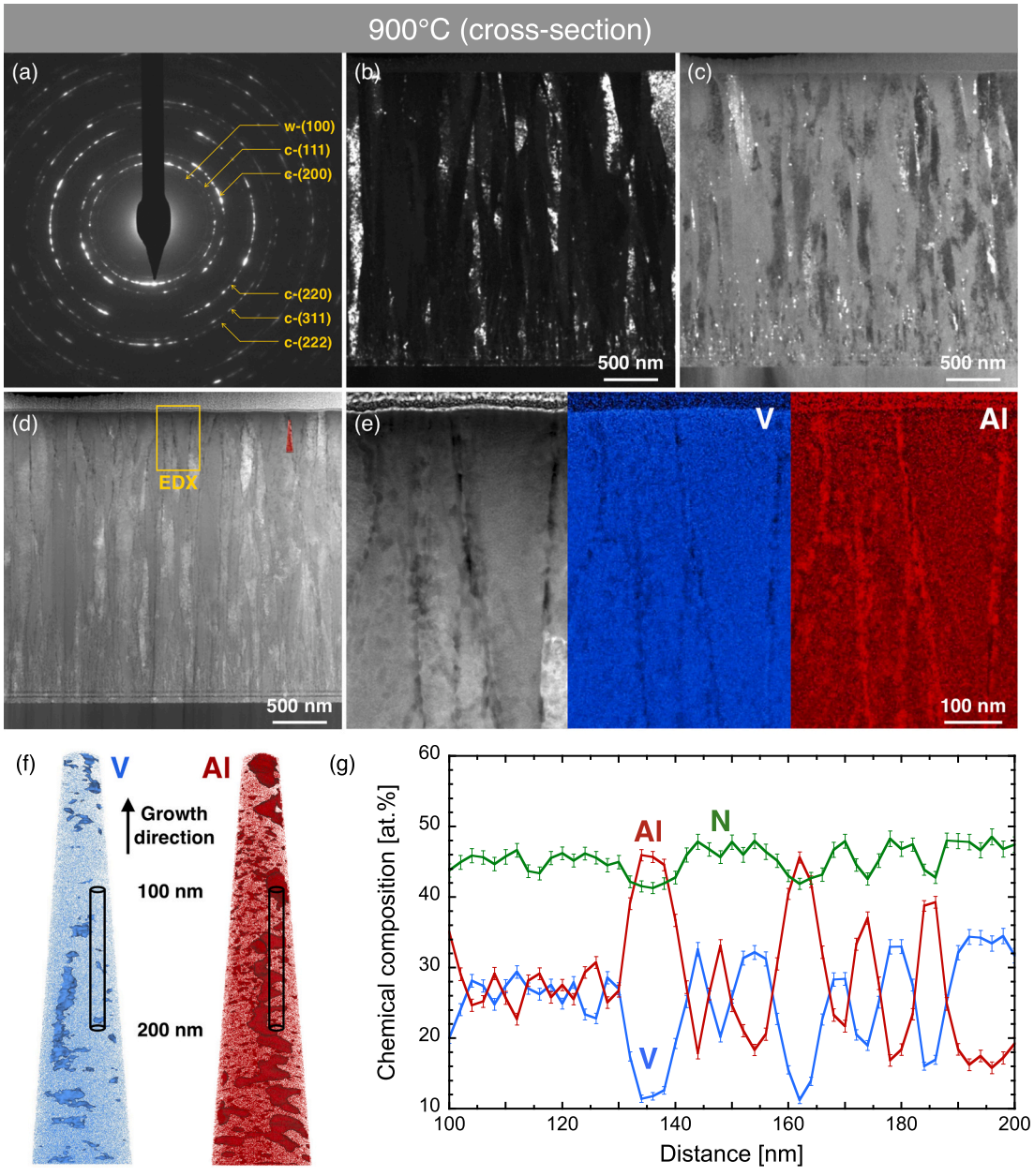

Fig. 5. Microstructure and local chemical composition after cyclic annealing at 900 °C (cross-section). (a) SAED pattern. (b) DF image taken with cubic (111) and (200) reflections. (c) DF image taken with wurtzite (100) reflections. (d) HAADF image. (e) HAADF and STEM-EDX elemental maps of V and Al. The region of interest is indicated in (d). (f) APT reconstruction of V and Al atomic positions. V- and Al-rich regions, both with ≥40 at.%, are highlighted by isoconcentration surfaces. (g) Chemical composition profile from the cylinder with dimensions of 10 × 10 × 100 nm indicated in (f).

4.3. Mechanical and electrical properties

The evolution of mechanical and electrical properties after cyclic vacuum annealing is presented in Fig. 6. The elastic modulus increased slightly from 491 ± 18 GPa in the as deposited state to 520 ± 18 GPa after cyclic annealing at 600 °C (Fig. 6a). It is well known that the elastic modulus of metastable cubic transition metal aluminum nitride thin films is stress-dependent [45,46]. Thus, the higher elastic modulus upon cyclic annealing at 600 °C can be understood by considering the residual stress state changes from −3.6 ± 0.6 to −6.0 ± 0.5 GPa (Fig. 6b). The larger compressive residual stress after annealing at 600 °C may be caused by the formation of coherency strains [13] due to onset of spinodal decomposition already after annealing at 600 °C. The chemical composition modulations responsible for coherency strain formation are expected to be rather small and probably within the count rate statistics of the chemical composition profile shown in Fig. 2e. Moreover, it has been recently demonstrated that the spatial resolution of atom probe tomography imaging is limited so that neighborhood relationships after field evaporation and data reconstruction cannot be represented [47,48]. Hence, chemical composition modulations that may or may not be present in the here investigated (V,Al)N thin films on the order of 1 nm or below cannot be detected. Based on density functional theory predictions, the increase in compressive stress state after vacuum annealing at 600 °C should cause an enhancement of elastic modulus by approximately +20 GPa [6] which is in good agreement with the here observed +29 GPa, when taking into account the scattering of nanoindentation data. Higher annealing temperatures cause a decrease of the elastic modulus from 489 ± 29 GPa (800 °C) to 437 ± 28 GPa (900 °C). Moreover, the residual stress state changes from compressive (−1.4 ± 0.8 GPa) to tensile (1.7 ± 0.4 GPa), respectively, and has been predicted to cause a decrease of elastic modulus by approximately −30 GPa [6]. Hence, the average measured elastic modulus reduction by −52 GPa appears to be predominated by the residual stress state.

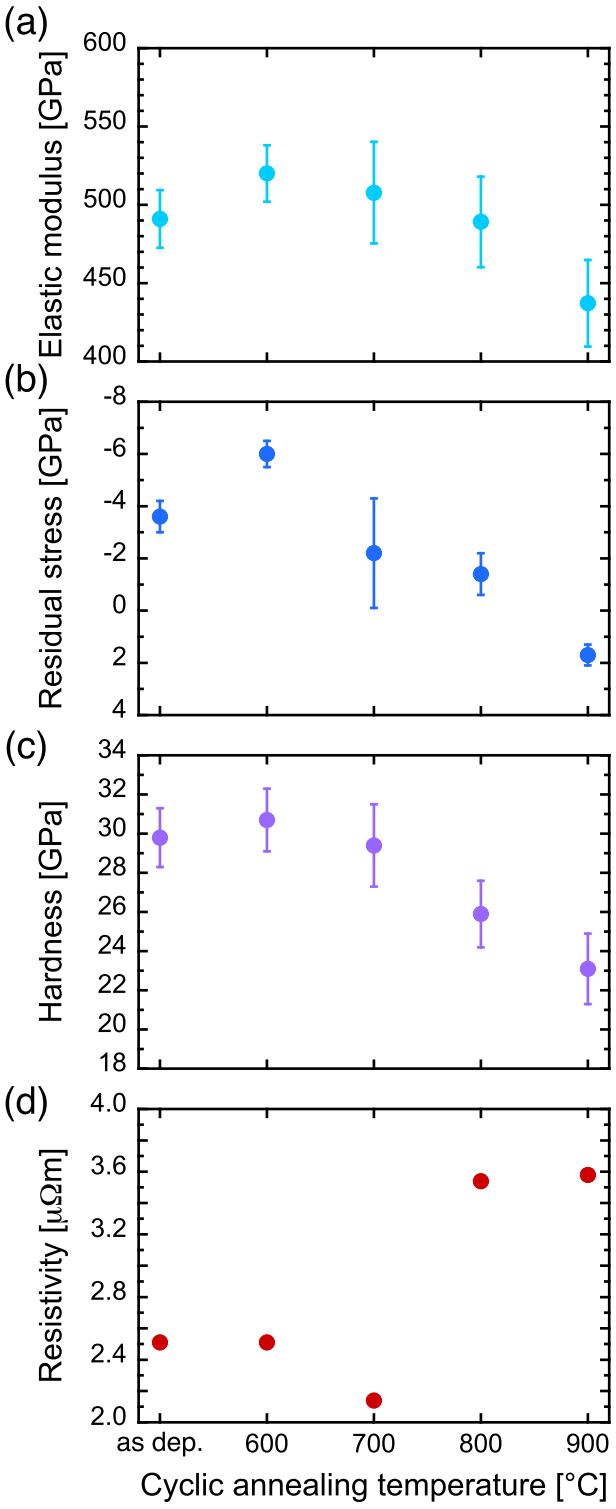

Fig. 6. Mechanical and electrical properties for different cyclic annealing temperatures. (a) Elastic modulus, (b) residual stress state, (c) hardness, (d) resistivity.

While age hardening has been reported for (Ti,Al)N [13], the hardness of as deposited (V,Al)N is 30 ± 2 GPa and not affected by the onset of spinodal decomposition at 700 °C (Fig. 6c). Age hardening in (Ti,Al)N has been explained by lattice distortions which are induced by coherency strains [13,49], while large strain formation can be understood by the 4.4% volume mismatch of TiN and cubic AlN [50]. Based on the significantly lower volume mismatch of 1.2% between VN and cubic AlN [15], strain-induced age hardening of spinodally-decomposed (V,Al)N appears to be negligible. At higher temperatures a significant hardness decrease from 29 ± 2 GPa (700 °C) to 23 ± 2 GPa (900 °C) is evident and caused by the wurtzite phase formation [51] and related structural changes at the grain boundaries. The 22% hardness reduction after cyclic annealing at 900 °C in comparison to the as deposited state is more distinct than the 11% reduction of elasticity. It has to be considered that the plastic zone radius [52] for the here employed measurement conditions is in the range of 0.7 to 1.3 μm, while the elastic strain field radius [53] is approximately factor two higher. While thermally-induced decomposition is more pronounced within the first 1 μm from the thin film surface, which is on the same order as the plastic zone, the entire thin film contributes to the measured elasticity.

The resistivity of 2.5 μΩm was obtained for as deposited $(V_{0.64}Al_{0.36})_{0.49}N_{0.51}$ as well as after cyclic annealing at 600 °C (Fig. 6d). It is well known that the resistivity is significantly affected by the aluminum concentration as 0.35 and 5.3 μΩm were reported for magnetron-sputtered TiN [54] and arc-deposited $Ti_{0.53}Al_{0.47}N$ [46], respectively. Wurtzite AlN is a wide bandgap semiconductor (band gap >6 eV [55]) and the resistivity of 10^{20} μΩm was reported for single-crystal epitaxial AlN thin films [56] which is 19 orders of magnitude higher than the here obtained resistivity values. While the resistivity of (V,Al)N decreases to 2.1 μΩm after annealing at 700 °C, the formation of the wurtzite phase, unambiguously identified by microscopy and tomography, is visible for temperatures ≥800 °C as the resistivity is increased to 3.6 μΩm, while percolation is not reached. Since wurtzite AlN is only formed at grain boundaries after cyclic vacuum annealing at 800 °C (see Fig. 4f), it is evident that resistivity measurements are sensitive to these structural changes. In contrast, the elastic modulus appears to be governed by the residual stress state and a hardness reduction is only observed after annealing at 900 °C.

4.4. Mobility on the metal sublattice

The mobility of aluminum and vanadium has been evaluated by density functional theory predictions of bulk diffusion barriers, E_b (Fig. 7a). It turns out that the migration barriers, ultimately controlling the diffusion rate of individual species, strongly depend on the composition and already at $x = 0.25$ aluminum exhibits a 25% lower activation energy for bulk diffusion compared to vanadium. The barriers for all species increase monotonically with increasing aluminum content. This is partly related to the smaller lattice constants for increasing x in $V_{1-x}Al_xN$, i.e. smaller space for the jumping atoms. Importantly, aluminum exhibits systematically smaller E_b than vanadium (and nitrogen) suggesting that the diffusion rate of aluminum is larger than that of vanadium and nitrogen.

The formation or presence of vacancies is a prerequisite for mobility on the sublattices. Nitrogen overstoichiometry [37] of the $(V_{0.64}Al_{0.36})_{0.49}N_{0.51}$ films as well as the likely formation of Frenkel pairs [36] point towards the existence of vacancies on the metallic sublattice; the concentration of metal vacancies (i.e. sites where vanadium and aluminum can jump) is related to the ratio of vanadium and aluminum atoms on the metal sublattice (approx. 2:1), the ratio between metal and non-metal species as well as the respective vacancy formation energies. Additional vacancies will be generated thermally. Their amount in turn depends on the vacancy formation energies, E_f (Fig. 7b). Lower E_f of vanadium than of aluminum vacancies implies higher amount of vanadium than aluminum vacancies. Nevertheless, estimating their amount using $\exp.(-E_f/k_BT)$ leads to values on the order 10^{-8} and lower, i.e. more than six orders of magnitude smaller than the amount of structural vacancies as estimated by assuming that the nitrogen overstoichiometry is balanced by the formation of metal vacancies. Therefore, it is reasonable to assume that the overall mass transport is dominated by the bulk diffusion barriers, favoring the mobility of aluminum over vanadium. We note that this trend is significant enough to preserve even if local stresses in nanocrystalline materials are considered.

4.5. Critical decomposition mechanism for the mechanical properties

From the here presented data it is evident that both spinodal decomposition of (V,Al)N into V- and Al-rich cubic nitride phases as well as diffusion of aluminum to grain boundaries and triple junctions are initiated concurrently after cyclic annealing at 700 °C. However, the hardness of 29 ± 2 GPa at 700 °C is as high as in the as deposited state and a reduction to 23 ± 2 GPa occurs only at 900 °C in accordance with the detection of wurtzite AlN by X-ray diffraction (Fig. 1). Unambiguous evidence for wurtzite phase formation is obtained after cyclic vacuum annealing at 800 °C by transmission electron microscopy and atom probe tomography data. The volume fraction of the wurtzite phase after annealing at 800 °C is very small and these regions are present only in the surface-near region (<500 nm) of the thin films. The subsequent annealing cycle at 900 °C caused growth of the wurtzite phase to such extent that it is also visible from diffraction data. Hence, it can be understood that the thermal stability of (V,Al)N is limited by the intercolumnar high angle grain boundaries where aluminum diffusion leads to the formation of wurtzite AlN.

The mechanism of wurtzite AlN formation is illustrated in Fig. 8. The plan-view HAADF image as well as the elemental map after cyclic vacuum annealing at 700 °C (Fig. 8a) show aluminum segregations at the triple junctions, surrounded by regions enriched in vanadium. In addition, the grain boundaries are Al-depleted in vicinity of the triple junctions. Based on the ab initio calculated jump barriers, favoring aluminum as species with larger diffusion rate than vanadium, it appears that the underdense grain boundaries serve as diffusion channels for aluminum. Hence, it can be understood that aluminum diffuses first to the grain boundaries and subsequently via the boundary to the junctions (a reasonable diffusion path is indicated by arrows in Fig. 8a). The 28% larger volume (per formula unit) of wurtzite AlN compared to cubic AlN [13] can explain the initial formation of wurtzite AlN at triple junctions due to their large volume. It should be noticed that aluminum diffusion at 700 °C occurs only locally as there are also chemically homogeneous grain boundaries present (dashed rectangle in Fig. 8a). After cyclic vacuum annealing at 800 °C there are aluminum segregations at the grain boundaries visible (Fig. 8b) and wurtzite AlN formation occurs at the triple junctions (compare Fig. 4). In contrast to the intercolumnar high angle grain boundaries, twin boundaries are entirely enriched in vanadium (Fig. 8b).

Significant aluminum enrichment at the grain boundaries was also identified in $Ti_{0.46}Al_{0.54}N$ films with columnar grains after annealing at 900 °C for 1 min, concurrently to spinodal decomposition [57]. Based on the strain evolution in $Ti_{0.53}Al_{0.47}N$ with columnar microstructure, it has been suggested that small domains of the wurtzite phase are formed already in the early stages of decomposition [58]. Furthermore, the preferred formation of wurtzite AlN domains was found at triple junctions of (Ti,Al)(O,N) coatings [42]. Moreover, in case of AlN/CrN superlattice thin films, annealed in Ar at 900 °C, evidence for the formation of nanocrystalline wurtzite AlN at grain boundary junctions was demonstrated by transmission electron microscopy and atom probe

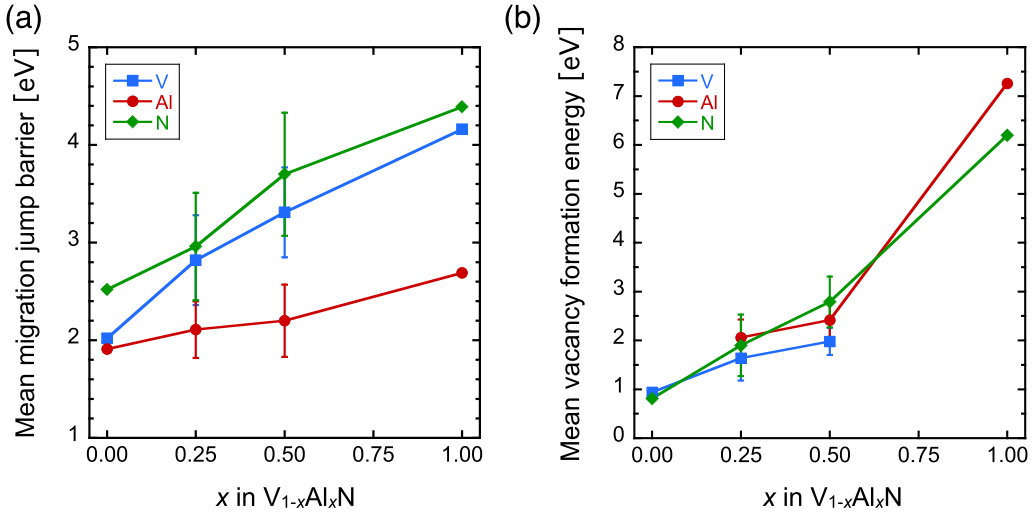

Fig. 7. (a) Migration jump barriers, E_b, and (b) vacancy formation energies, E_f, for V, Al and N as a function of x in $V_{1-x}Al_xN$. The shown data were obtained as mean values and corresponding standard deviations of all possible scenarios in the respective supercell.

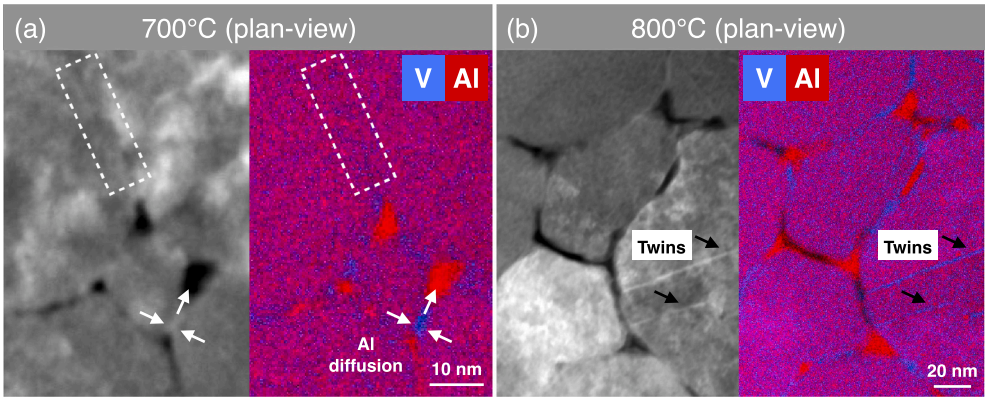

Fig. 8. Plan-view HAADF and STEM-EDX elemental maps of V and Al after cyclic vacuum annealing at (a) 700 and (b) 800 °C. The white arrows indicate a reasonable Al diffusion path in a grain boundary after annealing at 700 °C, while the dashed rectangle highlights a chemically homogeneous grain boundary in (a). The presence of V-rich twin boundaries is highlighted by black arrows in the image of the film annealed at 800 °C (b).

tomography [40]. Thus, it can be concluded that the thermal stability of metastable transition metal aluminum nitride thin films with cubic crystal structure is in general limited by the presence of columnar grain boundaries. Due to the higher mobility of aluminum compared to transition metals, aluminum can diffuse to the grain boundaries and causes deterioration of the mechanical properties by formation of wurtzite AlN.

5. Conclusions

The thermal decomposition of single-phase metastable cubic (V,Al)N thin films with columnar microstructure was systematically studied by a combination of vacuum annealing from 600 to 900 °C and subsequent characterization by X-ray diffraction, transmission electron microscopy, atom probe tomography, nanoindentation as well as resistivity measurements. The onset of spinodal decomposition into isostructural V- and Al-rich cubic nitride phases has been demonstrated after cyclic vacuum annealing at 700 °C. Moreover, at this temperature evidence for aluminum diffusion to grain boundaries and triple junctions is provided by correlation of transmission electron microscopy and atom probe tomography data. The formation of Al-rich regions can be understood by the more than 25% lower activation energy for bulk diffusion of aluminum compared to vanadium as obtained from ab initio calculations. It is reasonable to assume that these Al-rich regions are precursors for the formation of wurtzite AlN, which is unambiguously identified after annealing at 800 °C by microscopy and tomography. The significantly larger equilibrium volume of wurtzite AlN compared to the cubic phase explains its initial formation exclusively at triple junctions and grain boundaries. In contrast to the intercolumnar high angle grain boundaries, twin boundaries are entirely enriched in vanadium. Interestingly, the formation of the wurtzite phase at grain boundaries and triple junctions can be tracked by resistivity measurements as well. Based on diffraction, hardness and elastic modulus data, the onset of wurtzite AlN phase formation is identified after annealing at 900 °C. Hence, the onset temperature of wurtzite phase formation is characterization technique-dependent with a range of <800 °C (precursors of the wurtzite phase may have already formed after annealing at 700 °C) to ≤900 °C for (V,Al)N. It is evident that the formation temperatures of wurtzite AlN reported in the literature determined by other characterization techniques than chemical and structural characterization at the nanometer scale and/or resistivity measurements are overestimated.

Declaration of competing interest

The authors declare that they have no known competing financial interests or personal relationships that could have appeared to influence the work reported in this paper.

Acknowledgments

This research was funded by German Research Foundation (DFG, SFB-TR 87/3) “Pulsed high power plasmas for the synthesis of nanostructured functional layers”, European Structural and Investment Funds (VEKOP-2.3.3-15-2016-00002 and VEKOP-2.3.2-16-2016-00011) and the joined project of Austrian Science Fund (FWF, I 4059-N36) and Czech Science Foundation (19-29679L). The computational results have been achieved in part using the Vienna Scientific Cluster (VSC).

Appendix A. Supplementary data

Supplementary data to this article can be found online at https://doi.org/10.1016/j.surfcoat.2022.128235.

References

[1] W.-D. Münz, Titanium aluminum nitride films: a new alternative to TiN coatings, J. Vac. Sci. Technol. A 4 (1986) 2717–2725, https://doi.org/10.1116/1.573713.
[2] O. Knotek, W.-D. Münz, T. Leyendecker, Industrial deposition of binary, ternary and quaternary nitrides of titanium, zirconium and aluminum, J. Vac. Sci. Technol. A 5 (1987) 2173–2179, https://doi.org/10.1116/1.574948.
[3] H. Holleck, Design of nanostructured thin films for tribological applications, in: A. Kumar, Y.-W. Chung, J.J. Moore, J.E. Smugeresky (Eds.), Surface Engineering: Science and Technology I, The Minerals, Metals and Materials Society, Warrendale, 1999, pp. 207–218.
[4] S.J. Rotert, D. Music, M. to Baben, J.M. Schneider, Theoretical study of elastic properties and phase stability of $M_{0.5}Al_{0.5}N_{1-x}O_x$ (M = Sc, Ti, V, Cr), J. Appl. Phys. 113 (2013), https://doi.org/10.1063/1.4793496, 083512.
[5] D. Holec, M. Friák, J. Neugebauer, P.H. Mayrhofer, Trends in the elastic response of binary early transition metal nitrides, Phys. Rev. B 85 (2012), 064101, https://doi.org/10.1103/PhysRevB.85.064101.
[6] H. Rueß, D. Music, A. Bahr, J.M. Schneider, Effect of chemical composition, defect structure, and stress state on the elastic properties of $(V_{1-x}Al_x)_{1-y}N_y$, J. Phys. Condens. Matter 32 (2020), https://doi.org/10.1088/1361-648X/ab46df, 025901.
[7] H. Ju, P. Jia, J. Xu, L. Yu, Y. Geng, Y. Chen, M. Liu, T. Wei, The effects of adding aluminum on crystal structure, mechanical, oxidation resistance, friction and wear properties of nanocomposite vanadium nitride hard films by reactive magnetron sputtering, Mater. Chem. Phys. 215 (2018) 368–375, https://doi.org/10.1016/j.matchemphys.2018.05.061.
[8] P. Zhu, F. Ge, S. Li, Q. Xue, F. Huang, Microstructure, chemical states, and mechanical properties of magnetron co-sputtered $V_{1-x}Al_xN$ coatings, Surf. Coat. Technol. 232 (2013) 311–318, https://doi.org/10.1016/j.surfcoat.2013.05.023.
[9] N. Norrby, M.P. Johansson, R. M'Saoubi, M. Odén, Pressure and temperature effects on the decomposition of arc evaporated Ti0.6Al0.4N coatings in continuous turning, Surf. Coat. Technol. 209 (2012) 203–207, https://doi.org/10.1016/j.surfcoat.2012.08.068.
[10] M. Hillert, A solid-solution model for inhomogeneous systems, Acta Metall. 9 (1961) 525–535, https://doi.org/10.1016/0001-6160(61)90155-9.
[11] J.W. Cahn, On spinodal decomposition, Acta Metall. 9 (1961) 795–801, https://doi.org/10.1016/0001-6160(61)90182-1.

[12] A. Kimura, H. Hasegawa, K. Yamada, T. Suzuki, Effects of Al content on hardness, lattice parameter and microstructure of $Ti_{1-x}Al_xN$ films, Surf. Coat. Technol. 120-121 (1999) 438–441, https://doi.org/10.1016/S0257-8972(99)00491-0.

[13] P.H. Mayrhofer, A. Hörling, L. Karlsson, J. Sjölén, T. Larsson, C. Mitterer, L. Hultman, Self-organized nanostructures in the Ti-Al-N system, Appl. Phys. Lett. 83 (2003) 2049–2051, https://doi.org/10.1063/1.1608464.

[14] E. Wang, F. Ge, P. Zhu, P. Li, F. Meng, R. Shu, J. Yue, F. Huang, Age hardening of magnetron sputtered V-Al-Si-N quaternary coatings, Surf. Coat. Technol. 324 (2017) 429–437, https://doi.org/10.1016/j.surfcoat.2017.05.064.

[15] M. Hans, H. Rueß, Z. Czigány, J. Krause, P. Ondračka, D. Music, S. Evertz, D. M. Holzapfel, D. Primetzhofer, J.M. Schneider, Spinodal decomposition of reactively sputtered $(V_{0.64}Al_{0.36})_{0.49}N_{0.51}$ thin films, Surf. Coat. Technol. 389 (2020) 125641, https://doi.org/10.1016/j.surfcoat.2020.125641.

[16] G. Greczynski, S. Mráz, L. Hultman, J.M. Schneider, Venting temperature determines the surface chemistry of magnetron sputtered TiN films, Appl. Phys. Lett. 108 (2016), 041603, https://doi.org/10.1063/1.4940974.

[17] B.D. Cullity, Elements of X-ray Diffraction, second ed., Addison-Wesley, Reading, 1956.

[18] M. Birkholz, Thin Film Analysis by X-ray Scattering, WILEY-VCH, Weinheim, 2006.

[19] B.D. Fulcher, X.Y. Cui, B. Delley, C. Stampfl, Hardness analysis of cubic metal mononitrides from first principles, Phys. Rev. B 85 (2012), 184106, https://doi.org/10.1103/PhysRevB.85.184106.

[20] W.C. Oliver, G.M. Pharr, An improved technique for determining hardness and elastic modulus using load and displacement sensing indentation experiments, J. Mater. Res. 7 (1992) 1564–1583, https://doi.org/10.1557/JMR.1992.1564.

[21] G.M. Pharr, W.C. Oliver, F.R. Brotzen, On the generality of the relationship among contact stiffness, contact area, and elastic modulus during indentation, J. Mater. Res. 7 (1992) 613–617, https://doi.org/10.1557/JMR.1992.0613.

[22] L.J. Van der Pauw, A method of measuring the resistivity and Hall coefficient on lamellae of arbitrary shape, Philips Tech. Rev. 20 (1958) 220–224.

[23] K. Thompson, D. Lawrence, D.J. Larson, J.D. Olson, T.F. Kelly, B. Gorman, In situ site-specific specimen preparation for atom probe, Ultramicroscopy 107 (2007) 131–139, https://doi.org/10.1016/j.ultramic.2006.06.008.

[24] M. Hans, J.M. Schneider, Electric field strength-dependent accuracy of TiAlN thin film composition measurements by laser-assisted atom probe tomography, New J. Phys. 22 (2020), 033036, https://doi.org/10.1088/1367-2630/ab7770.

[25] M. Hans, J.M. Schneider, On the chemical composition of TiAlN thin films - comparison of ion beam analysis and laser-assisted atom probe tomography with varying laser pulse energy, Thin Solid Films 688 (2019), 137251, https://doi.org/10.1016/j.tsf.2019.04.026.

[26] G. Kresse, J. Furthmüller, Efficiency of ab-initio total energy calculations for metals and semiconductors using a plane-wave basis set, Comput. Mater. Sci. 6 (1996) 15–50, https://doi.org/10.1016/0927-0256(96)00008-0.

[27] G. Kresse, J. Furthmüller, Efficient iterative schemes for ab initio total-energy calculations using a plane-wave basis set, Phys. Rev. B 54 (1996) 11169, https://doi.org/10.1103/PhysRevB.54.11169.

[28] J.P. Perdew, K. Burke, M. Ernzerhof, Generalized gradient approximation made simple, Phys. Rev. Lett. 77 (1996) 3865, https://doi.org/10.1103/PhysRevLett.77.3865.

[29] P.E. Blöchl, Projector augmented-wave method, Phys. Rev. B 50 (1994) 17953, https://doi.org/10.1103/PhysRevB.50.17953.

[30] S.-H. Wei, L.G. Ferreira, J. Bernard, A. Zunger, Electronic properties of random alloys: special quasirandom structures, Phys. Rev. B 42 (1990) 9622–9649, https://doi.org/10.1103/PhysRevB.42.9622.

[31] H.J. Monkhorst, J.D. Pack, Special points for Brillouin-zone integrations, Phys. Rev. B 13 (1976) 5188, https://doi.org/10.1103/PhysRevB.13.5188.

[32] M. Methfessel, A.T. Paxton, High-precision sampling for Brillouin-zone integration in metals, Phys. Rev. B 40 (1989) 3616, https://doi.org/10.1103/PhysRevB.40.3616.

[33] D. Sheppard, R. Terrell, G. Henkelman, Optimization methods for finding minimum energy paths, J. Chem. Phys. 128 (2008), 134106, https://doi.org/10.1063/1.2841941.

[34] M. Bartosik, D. Holec, D. Apel, M. Klaus, C. Genzel, J. Keckes, M. Arndt, P. Polcik, C.M. Koller, P.H. Mayrhofer, Thermal expansion of Ti-Al-N and Cr-Al-N coatings, Scr. Mater. 127 (2017) 182–185, https://doi.org/10.1016/j.scriptamat.2016.09.022.

[35] M. to Baben, L. Raumann, J.M. Schneider, Phase stability and elastic properties of titanium aluminum oxynitride studied by ab initio calculations, J. Phys. D. Appl. Phys. 46 (2013), https://doi.org/10.1088/0022-3727/46/8/084002, 084002.

[36] S.K. Aghda, D. Music, Y. Unutulmazsoy, H.H. Sua, S. Mráz, M. Hans, D. Primetzhofer, A. Anders, J.M. Schneider, et al., Acta Mater. 214 (2021), 117003, https://doi.org/10.1016/j.actamat.2021.117003.

[37] M. to Baben, M. Hans, D. Primetzhofer, S. Evertz, H. Rueß, J.M. Schneider, Unprecedented thermal stability of inherently metastable aluminum nitride by point defect engineering, Mater. Res. Lett. 5 (2017) 158–169, https://doi.org/10.1080/21663831.2016.1233914.

[38] I. Petrov, P.B. Barna, L. Hultman, J.E. Greene, Microstructural evolution during film growth, J. Vac. Sci. Technol. A 21 (2003), https://doi.org/10.1116/1.1601610. S217-S128.

[39] B. Gault, D.W. Saxey, M.W. Ashton, S.B. Sinnott, A.N. Chiaramonti, M.P. Moody, D. K. Schreiber, Behavior of molecules and molecular ions near a field emitter, New J. Phys. 18 (2016), 033031, https://doi.org/10.1088/1367-2630/18/3/033031.

[40] D. Tytko, P.-P. Choi, D. Raabe, Thermal dissolution mechanisms of AlN/CrN hard coating superlattices studied by atom probe tomography and transmission electron microscopy, Acta Mater. 85 (2015) 32–41, https://doi.org/10.1016/j.actamat.2014.11.004.

[41] K.P. Shaha, H. Rueß, S. Rotert, M. to Baben, D. Music, J.M. Schneider, Nonmetal sublattice population induced defect structure in transition metal aluminum oxynitrides, Appl. Phys. Lett. 103 (2013) 221905, https://doi.org/10.1063/1.4833835.

[42] D.M. Holzapfel, D. Music, M. Hans, S. Wolff-Goodrich, D. Holec, D. Bogdanovski, M. Arndt, A.O. Eriksson, K. Yalamanchili, D. Primetzhofer, C.H. Liebscher, J. M. Schneider, Enhanced thermal stability of (Ti,Al)N coatings by oxygen incorporation, Acta Mater. 218 (2021), 117204, https://doi.org/10.1016/j.actamat.2021.117204.

[43] Z. Xu, Z. Zhang, M. Bartosik, Y. Zhang, P.J. Mayrhofer, Y. He, Insight into the structural evolution during TiN film growth via atomic resolution TEM, J. Alloys Compd. 754 (2018) 257–267, https://doi.org/10.1016/j.jallcom.2018.04.268.

[44] Y. Zhang, Z.-R. Liu, D.-W. Yuan, Q. Shao, J.-H. Chen, C.-L. Wu, Z.-L. Zhang, Elastic properties and stacking fault energies of borides, carbides and nitrides from first-principle calculations, Acta Metall. Sin. (Engl. Lett.) 32 (2019) 1099–1110, https://doi.org/10.1007/s40195-019-00873-8.

[45] D. Music, L. Banko, H. Ruess, M. Engels, A. Hecimovic, D. Grochla, D. Rogalla, T. Brögelmann, A. Ludwig, A. von Keudell, K. Bobzin, J.M. Schneider, Correlative plasma-surface model for metastable Cr-Al-N: Frenkel pair formation and influence of the stress state on the elastic properties, J. Appl. Phys. 121 (2017), 215108, https://doi.org/10.1063/1.4985172.

[46] M. Hans, L. Patterer, D. Music, D.M. Holzapfel, S. Evertz, V. Schnabel, B. Stelzer, D. Primetzhofer, B. Völker, B. Widrig, A.O. Eriksson, J. Ramm, M. Arndt, H. Rudigier, J.M. Schneider, Stress-dependent elasticity of TiAlN coatings, Coatings 9 (2019) 24, https://doi.org/10.3390/coatings9010024.

[47] F. De Geuser, B. Gault, Metrology of small particles and solute clusters by atom probe tomography, Acta Mater. 188 (2020) 406–415, https://doi.org/10.1016/j.actamat.2020.02.023.

[48] B. Gault, B. Klaes, F.F. Morgado, C. Freysoldt, Y. Li, F. De Geuser, L.T. Stephenson, F. Vurpillot, Reflections on the spatial performance of atom probe tomography in the analysis of atomic neighbourhoods, Microsc. Microanal. (2021) 1–11, https://doi.org/10.1017/S1431927621012952.

[49] A. Hörling, L. Hultman, M. Odén, J. Sjölén, L. Karlsson, Thermal stability of arc evaporated high aluminum-content $Ti_{1-x}Al_xN$ thin films, J. Vac. Sci. Technol. A 20 (2002) 1815–1823, https://doi.org/10.1116/1.1503784.

[50] P.H. Mayrhofer, D. Music, J.M. Schneider, Influence of the Al distribution on the structure, elastic properties, and phase stability of supersaturated $Ti_{1-x}Al_xN$, J. Appl. Phys. 100 (2006), 094906, https://doi.org/10.1063/1.2360778.

[51] G. Greczynski, S. Mráz, M. Hans, D. Primetzhofer, J. Lu, L. Hultman, J. M. Schneider, Unprecedented Al supersaturation in single-phase rock salt structure VAlN films by Al+ subplantation, J. Appl. Phys. 121 (2017), 171907, https://doi.org/10.1063/1.4977813.

[52] J. Chen, S.J. Bull, On the relationship between plastic zone radius and maximum depth during nanoindentation, Surf. Coat. Technol. 201 (2006) 4289–4293, https://doi.org/10.1016/j.surfcoat.2006.08.099.

[53] S. Bec, A. Tonck, J.-L. Loubet, A simple guide to determine elastic properties of films on substrate from nanoindentation experiments, Philos. Mag. 86 (2006) 5347–5358, https://doi.org/10.1080/14786430600660856.

[54] B. Stelzer, M. Momma, J.M. Schneider, Autonomously self-reporting hard coatings: tracking the temporal oxidation behavior of TiN by in situ sheet resistance measurements, Adv. Funct. Mater. 30 (2020) 2000146, https://doi.org/10.1002/adfm.202000146.

[55] P.B. Perry, R.F. Rutz, The optical absorption edge of single-crystal AlN prepared by a close-spaced vapor process, Appl. Phys. Lett. 33 (1978) 319–321, https://doi.org/10.1063/1.90354.

[56] K. Tsubouchi, N. Mikoshiba, Zero-temperature-coefficient SAW devices on AlN epitaxial films, IEEE Trans. Sonics Ultrason. 32 (1985) 634–644, https://doi.org/10.1109/T-SU.1985.31647.

[57] R. Rachbauer, S. Massl, E. Stergar, D. Holec, D. Kiener, J. Keckes, J. Patscheider, M. Stiefel, H. Leitner, P.H. Mayrhofer, Decomposition pathways in age hardening of Ti-Al-N films, J. Appl. Phys. 110 (2011), 023515, https://doi.org/10.1063/1.3610451.

[58] L. Rogström, J. Ullbrand, J. Almer, L. Hultman, B. Jansson, M. Odén, Strain evolution during spinodal decomposition of TiAlN thin films, Thin Solid Films 520 (2012) 5542–5549, https://doi.org/10.1016/j.tsf.2012.04.059.